aerospace

MDPI

Article

A Constant Power Reaching Law for Intelligent Attitude Fault-Tolerant Control of Launch Vehicles

Xi Tong [1,*], Wenxing Fu [2] and Jie Yan [2]

[1] School of Astronautics, Northwestern Polytechnical University, 127 West Youyi Road, Beilin District, Xi'an 710072, China
[2] Unmanned System Research Institute, Northwestern Polytechnical University, 127 West Youyi Road, Beilin District, Xi'an 710072, China; wenxingfu@nwpu.edu.cn (W.F.); jyan@nwpu.edu.cn (J.Y.)
* Correspondence: tongxi92@mail.nwpu.edu.cn; Tel.: +86-186-2957-8621

Abstract

Sliding Mode Control (SMC) is a widely used controlling method in the field of current attitude control of launch vehicles. The effectiveness of reaching the Sliding Surface could influence the effect of the attitude control. Aiming to derive better control quality of attitude angles to launch vehicles by investigating the correlation between rise time, maximum overshoot, settling time, respond speed, and motion smoothness, a novel Comprehensive Evaluation Index Function (CEIF) was designed for balancing response speed and motion smoothness. Further, based on this CEIF, both the control characters influenced by the Constant Reaching Law and those characters influenced by the Power Reaching Law were used to propose the Constant Power Reaching Law (CPRL). Then, a fast terminal sliding mode controller was developed. In the simulation, regardless of when the launch vehicle attitude faults occurred, the CEIF with Monotonic Increase in Each Independent Variable could clearly and accurately represent the control quality of launch vehicle attitude. The fast terminal sliding mode controller (FTSM controller) with CPRL could provide better quality of attitude fault-tolerant control compared with a series of FTSM controllers with different currently established reaching laws.

Keywords: launch vehicle; fault-tolerant control; reaching law; CEIF

1. Introduction

The launch vehicle is very important in the entire spacecraft transportation system. Since the fulfilment of orbital insertion accuracy specifications of the launch vehicle is inevitably influenced by various inner and outer disturbances, flight control of the launch vehicle becomes indispensable [1]. Finite time attitude stabilization of a reentry reusable launch vehicle [2] and the attitude control problem of VTVL RLV in the attitude adjustment phase [3] have been investigated with the help of Sliding Mode Control (SMC). Actually, Sliding Mode Variable Structure Control (i.e, SMC) exhibits strong applicability, being suitable for both linear and nonlinear systems, as well as continuous or discrete systems. By switching the control inputs, it drives the system states to converge toward and then slide along the predefined sliding surface, thereby demonstrating strong robustness against external disturbances. As a model-based control method that is as typical as Adaptive Control, it has been widely applied in fields including launch vehicle attitude control [4]. The safety of launch vehicle flight control is still challenged [5,6]. Fault-tolerant control strategies are increasingly widely applied in the design of flight control systems of spacecraft for their

Check for updates

Academic Editor: Paolo Teofilatto

Received: 4 January 2026
Revised: 27 February 2026
Accepted: 2 March 2026
Published: 11 March 2026

Copyright: © 2026 by the authors. Licensee MDPI, Basel, Switzerland. This article is an open access article distributed under the terms and conditions of the Creative Commons Attribution (CC BY) license.

ability to implement measures, including regulation of parameters or reconfiguration with support of information about fault detection. Thanks to this ability, the stability of flight vehicles is restored and the essential capacity for control is preserved even in actuator fault occurrence [7,8].

The fault-tolerant controller design has become significant for the spacecraft attitude control system to effectively ensure the attitude control performance with faults in spacecraft. Adaptive technology, sliding mode control (SMC), control allocation and many others have been systematically utilized to achieve attitude fault-tolerant control. Especially, SMC techniques are a popular option in designing controller targeting at spacecraft actuator faults [9]. Additionally, an adaptive SMC algorithm was applied to Inner-Loop Controller Design as a vital part of attitude fault-tolerant control [10]. The motion of variable-structure SMC systems can be separated into a reaching phase and sliding phase. For system transient process quality to be better, the quality of the sliding phase can depend upon the sliding surface equation; various reaching laws are designed to improve the quality of the reaching phase, including Reaching Speed and Chattering [11]. Among traditional reaching laws, the Constant Reaching Law and Exponential Reaching Law respectively show invariable reaching speed and increasing reaching speed with system state distant from the sliding surface, but neither of them can theoretically eliminate chattering. Even the Power Reaching Law has eliminated chattering with zero velocity when reaching the sliding surface, and the reaching speed is still too low if the system state is far from the sliding surface [12]. To raise the convergence velocity of the system state, the double power reaching law was applied in [13]. Superior tracking accuracy in both position and velocity was achieved through a new reaching law of SMC formed using both a special power function and an inverse hyperbolic sine function adopted for an adaptive SMC law [14]. Chattering has been restrained using a novel variable exponential reaching law within a sliding mode variable structure control strategy [15], and with an improved Exponential Reaching Law in which the sign function can be adapted using fuzzy controller to design a fuzzy terminal sliding controller [16]. In addition, reaching the sliding surface with both high system state velocity and eliminating chattering could be achieved using a two-power reaching law provided in [17] and a multi-power reaching law of SMC provided in [18], whose targeted adjustment was implemented in different phases of the reaching process with three exponents of the Power Function Term.

Regardless of the effective enhancement of some performance indexes of dynamic response using the above reaching laws, most of these methods can only carry out qualitative analysis of these indexes without establishing well-defined metrics for control performance characterization of these reaching laws. This, along with a lack of compatibility between Respond Speed and Motion Smoothness, which could be respectively reflected by Rise Time t_r and its Maximum Overshoot σ_p, is regarded as a significant basis for correcting inaccuracies and improving steady-state performance of systems [19]. Therefore, a novel comprehensive evaluation index function (CEIF) F was proposed on the basis of Rise Time t_r, Maximum Overshoot σ_p and Settling time t_s of dynamic variation.

When the parameters of reaching law are given as some specific values, the term related to sign function in Constant Reaching Law achieved improvement in both Rise Time t_r and Maximum Overshoot σ_p, which even exert dominant influence on their whole improvement, especially when the attitude deviation caused by fault is relatively small. At the same time, the term related to the power function in the Power Reaching Law also achieves improvement in both of these two parameters. Therefore, when designing the reaching law, the term related to the sign function in the Constant Reaching Law and the term related to the power function in the Power Reaching Law are synthesized to achieve conflict resolution for compatibility between higher Respond Speed and better Fault

Damping Capability. Shown in the simulation results, through the comparison between the Constant Power Reaching Law (CPRL) and the other seven reaching laws, the value of CEIF related to the reaching law with the best related attitude control quality maintains the smallest both pre-failure and post-failure. Additionally, given specific constraints, higher response speed and better motion smoothness of the above dynamic variation can be maintained through a Fast Terminal Sliding Mode (FTSM) controller based on CPRL both pre-failure and post-failure.

In summary, the launch vehicle dynamics and kinematics are covered in Section 2.1. Section 2.2.1 covers the sliding surface equation. In Section 2.2.2, a novel CEIF is provided, and a CPRL is proposed in Section 2.2.3. The equation of a fault-tolerant control law based on FTSM is given in Section 2.2.4. Section 3 shows the analysis of the simulation results. Finally, the conclusion is presented in Section 4.

2. Method

2.1. Launch Vehicle Mathematical Model

The Equation of launch vehicle rotation around its center of mass can be expressed as follows:

$$\boldsymbol{J}\dot{\boldsymbol{\omega}} = -\boldsymbol{\Omega}\boldsymbol{J}\boldsymbol{\omega} + \boldsymbol{\tau} + \boldsymbol{d} \tag{1}$$

where $\boldsymbol{\tau} \in \mathbf{R}^3$ is the control torque, $\boldsymbol{d} = [d_x, d_y, d_z]^T \in \mathbf{R}^3$ is the composite interference term mainly including unmodeled dynamics, external interference and system uncertainty arising out of elastic mode, $\boldsymbol{J} = \text{diag}\,(J_{xx}, J_{yy}, J_{zz}) \in \mathbf{R}^{3\times3}$ is the inertia tensor (see Table A1 for details), $\boldsymbol{\omega} = [\omega_x, \omega_y, \omega_z]^T \in \mathbf{R}^3$ is the rotating angular rate (see Table A1 for details), and the matrix $\boldsymbol{\Omega}$ is as follows:

$$\boldsymbol{\Omega} = \begin{bmatrix} 0 & -\omega_z & \omega_y \\ \omega_z & 0 & -\omega_x \\ -\omega_y & \omega_x & 0 \end{bmatrix}$$

The attitude angles are defined as $\boldsymbol{\xi} = \left[\varphi, \psi, \theta\right]^T \in \mathbf{R}^3$, which includes rolling angle φ, yawing angle ψ and pitching angle θ, respectively (see Table A1 for details), and can be represented as follows:

$$\dot{\boldsymbol{\xi}} = \boldsymbol{S}(\boldsymbol{\xi})\boldsymbol{\omega} = \begin{bmatrix} 1 & \tan\psi\sin\varphi & \tan\psi\cos\varphi \\ 0 & \cos\varphi & -\sin\varphi \\ 0 & \sec\psi\sin\varphi & -\sec\psi\cos\varphi \end{bmatrix} \begin{bmatrix} \omega_x \\ \omega_y \\ \omega_z \end{bmatrix} \tag{2}$$

where $\boldsymbol{S}(\boldsymbol{\xi})$ is the coordinate transmission matrix [20].

The launch vehicle dynamic system, at its ascent stage, is mainly composed of four strap-on launch vehicle boosters expressed from A_1 to A_4 and two central launch vehicle engines expressed from B_1 to B_2, of which the four strap-on launch vehicle boosters can only make a single-axis motion, and the two central launch vehicle engines can make a dual-axis motion. The configuration of launch vehicle swinging actuators is shown in Figure 1.

In this figure, R_a and R_b represent the distances from the launch vehicle central axis (X-axis of the body frame) to the center of the strap-on launch vehicle boosters and to the center of the central launch vehicle engines, respectively. The angles of swinging deflections from their respective swinging centers of the strap-on launch vehicle boosters are expressed as $\delta_1 \sim \delta_4$, and the angles of swinging deflections from their respective swinging centers of the central launch vehicle engines are expressed as $\overline{\delta}_1 \sim \overline{\delta}_4$.

Applying the Launch Vehicle Swinging Angle Equivalent Principle, the swinging angles from each of the above thrusters could be transformed into Attitude Control Three Channel (Pitching, Yawing, Rolling) Equivalent Swinging Angle Command. This command could be expressed by equivalent swinging angle values $\boldsymbol{\delta} = [\delta_x, \delta_y, \delta_z]^T$ in the launch vehicle attitude control system at its ascent stage.

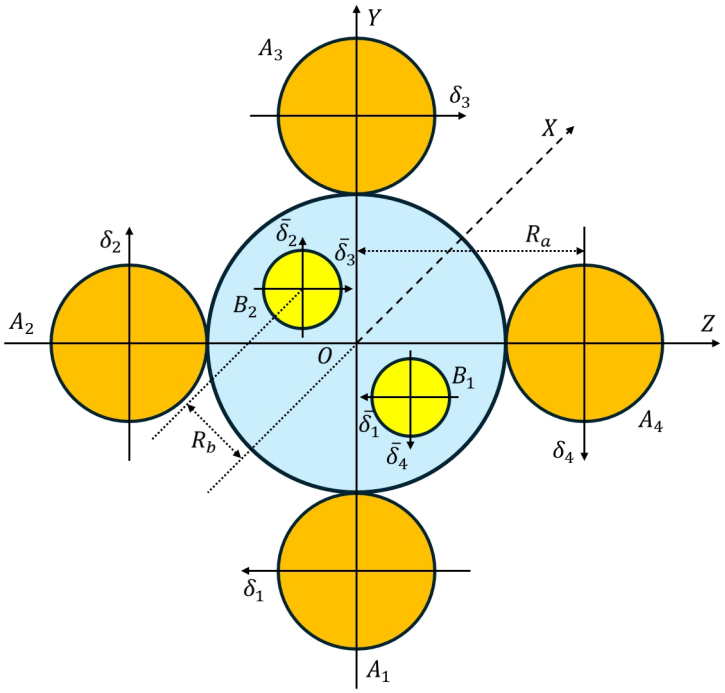


Figure 1. Configuration of Launch Vehicle Engines (View from Launch Vehicle Tail , mainly composed of four strap-on launch vehicle boosters expressed from A_1 to A_4 and two central launch vehicle engines expressed from B_1 to B_2, of which the four strap-on launch vehicle boosters can only make a single-axis motion, and the two central launch vehicle engines can make a dual-axis motion).

This paper chiefly studies the failure about the loss of effectiveness and the failure about deviation [20]. Therefore, the failure model of the actuator can be expressed in matrix form as follows:

$$\boldsymbol{\delta}_f = \boldsymbol{E}\boldsymbol{\delta} + \boldsymbol{\rho} \tag{3}$$

where $\boldsymbol{E} = \text{diag}\{e_1, e_2, e_3\} \in \boldsymbol{R}^{3\times3}$ satisfies $0 < e_i \leq 1 (i = 1, 2, 3)$, $\boldsymbol{\rho} = [\rho_1, \rho_2, \rho_3]^T$ [20] (see Table A1 for details). If $e_i = 0$, it means the i^{th} equivalent channel in these three ones has been completely out of control.

In Equation (3), $\boldsymbol{E} = \text{diag}\{e_1, e_2, e_3\} \in \boldsymbol{R}^{3\times3}$ satisfying $0 < e_i \leq 1 (i = 1, 2, 3)$ is the execution efficiency coefficient, and $\boldsymbol{\rho} = [\rho_1, \rho_2, \rho_3]^T$ is the bias fault coefficient.

The real control torque of the attitude control system [21] could be expressed as:

$$\boldsymbol{\tau}_f = \boldsymbol{G}\boldsymbol{\delta}_f \tag{4}$$

where the diagonal matrix $\boldsymbol{G} \in \boldsymbol{R}^{3\times3}$ is the torque transformation matrix.

Combining the above formulae, the launch vehicle attitude control system in its actuator fault condition can be expressed [20] as follows:

$$\begin{cases} \dot{\boldsymbol{\xi}} = \boldsymbol{S}(\boldsymbol{\xi})\boldsymbol{\omega} \\ \dot{\boldsymbol{\omega}} = \boldsymbol{J}^{-1}\left(-\boldsymbol{\Omega}\boldsymbol{J}\boldsymbol{\omega} + \boldsymbol{G}\boldsymbol{\delta}_f + \boldsymbol{d}\right) \\ \quad = -\boldsymbol{J}^{-1}\boldsymbol{\Omega}\boldsymbol{J}\boldsymbol{\omega} + \boldsymbol{J}^{-1}\boldsymbol{G}(\boldsymbol{E}\boldsymbol{\delta} + \boldsymbol{\rho}) + \boldsymbol{J}^{-1}\boldsymbol{d} \end{cases} \tag{5}$$

The tracking errors of the launch vehicle attitude system were defined as $\boldsymbol{x}_1 \triangleq \boldsymbol{\xi} - \boldsymbol{\xi}_c$ and $\boldsymbol{x}_2 \triangleq \dot{\boldsymbol{\xi}} - \dot{\boldsymbol{\xi}}_c$. $\boldsymbol{\xi}_c$ and $\dot{\boldsymbol{\xi}}_c$ are the attitude tracking instruction vector and the first-order derivative of this vector, respectively, so the launch vehicle attitude tracking system [20] can be expressed as follows:

$$\begin{cases} \dot{\boldsymbol{x}}_1 = \boldsymbol{x}_2 \\ \dot{\boldsymbol{x}}_2 = \dot{\boldsymbol{S}}(\boldsymbol{\xi})\boldsymbol{\omega} + \boldsymbol{S}(\boldsymbol{\xi})\dot{\boldsymbol{\omega}} - \ddot{\boldsymbol{\xi}}_c \\ = \left(\dot{\boldsymbol{S}} - \boldsymbol{S}\boldsymbol{J}^{-1}\boldsymbol{\Omega}\boldsymbol{J}\right)\boldsymbol{\omega} + \boldsymbol{S}\boldsymbol{J}^{-1}\boldsymbol{G}(\boldsymbol{E}\boldsymbol{\delta} + \boldsymbol{\rho}) + \boldsymbol{S}\boldsymbol{J}^{-1}\boldsymbol{d} - \ddot{\boldsymbol{\xi}}_c \end{cases} \tag{6}$$

Starting from the above equation, the coordinate transmission matrix $\boldsymbol{S}(\boldsymbol{\xi})$ was directly expressed as $\boldsymbol{S}$, which differed from the mathematical symbol $\boldsymbol{S}_{SMC}$ regarding the sliding mode control.

Let $\boldsymbol{G}_1 = \boldsymbol{S}\boldsymbol{J}^{-1}\boldsymbol{G}$, $\boldsymbol{F} = \left(\dot{\boldsymbol{S}} - \boldsymbol{S}\boldsymbol{J}^{-1}\boldsymbol{\Omega}\boldsymbol{J}\right)\boldsymbol{\omega} - \ddot{\boldsymbol{\xi}}_c$, $\boldsymbol{D} = \boldsymbol{S}\boldsymbol{J}^{-1}\boldsymbol{d}$, so Equation (6) was rewritten as follows:

$$\begin{cases} \dot{\boldsymbol{x}}_1 = \boldsymbol{x}_2 \\ \dot{\boldsymbol{x}}_2 = \boldsymbol{F} + \boldsymbol{G}_1\boldsymbol{E}\boldsymbol{\delta} + \boldsymbol{G}_1\boldsymbol{\rho} + \boldsymbol{D} \end{cases} \tag{7}$$

In the launch vehicle engine swing actuator fault condition shown in Equation (3), by designing a novel Reaching Law, a Fast Terminal Sliding Mode (FTSM) controller has been established in order to enhance the fault-tolerant control quality of the launch vehicle attitude control system, to diminish the negative impact of actuator faults and external interference, and to preserve the stability of the launch vehicle attitude system (5), which can be shown in the better parameter convergence in the instruction tracking error system (7).

2.2. Controller Design

The controller structure is shown in Figure 2. Based on the attitude angle information of the Launch Vehicle estimated by an adaptive fault observer, the fault-tolerant stability controller, with the help of both Terminal Sliding Mode Controlling, which could be equipped with a Constant Power Reaching Law (CPRL), and Radial Basis Function Neural Network (RBFNN), could control the engine actuators to operate the Launch Vehicle Dynamic Mode to track the Attitude Tracking Instruction. The algorithms still work, even though the fault information is input in the equation of the launch vehicle engine swing actuator.

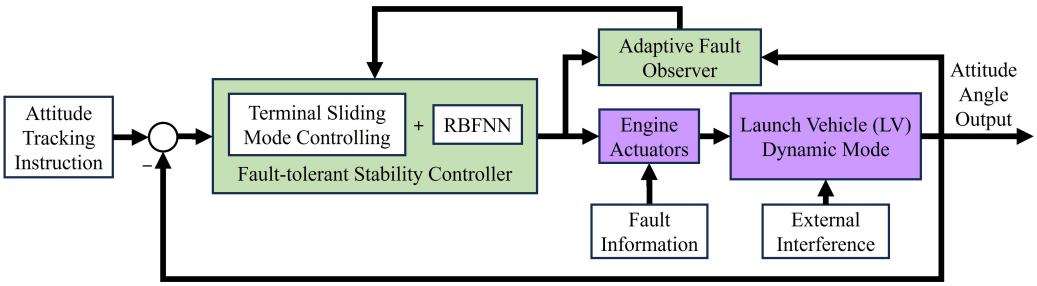


Figure 2. Intelligent fault-tolerant controller structure based on Terminal Sliding Mode theory and Radial Basis Function Network.

2.2.1. Sliding Surface Design

Firstly, as shown in Equation (8), the fast terminal sliding surface [22] was designed as follows:

$$\boldsymbol{S}_{SMC} = \hat{\boldsymbol{x}}_2 + \boldsymbol{l}_1\hat{\boldsymbol{x}}_1 + \boldsymbol{l}_2\overline{\boldsymbol{S}}(\hat{\boldsymbol{x}}_1) \tag{8}$$

In the above equation, $\boldsymbol{S}_{SMC} = \left[S_{SMC(1)}, S_{SMC(2)}, S_{SMC(3)}\right]^T \in \boldsymbol{R}^3$; $\boldsymbol{l}_1 = \text{diag}\{l_{11}, l_{12}, l_{13}\}$, $\boldsymbol{l}_2 = \text{diag}\{l_{21}, l_{22}, l_{23}\}$. $\hat{\boldsymbol{x}}_1$ and $\hat{\boldsymbol{x}}_2$ are the estimated values of $\boldsymbol{x}_1$ and $\boldsymbol{x}_2$, respectively. $\boldsymbol{l}_1$ and $\boldsymbol{l}_2$

are the main coefficient of the fast terminal sliding surface. Additionally, l_{1i} and $l_{2i}(i = 1,2,3)$ are positive constants. $\bar{\boldsymbol{S}} = [\bar{S}_1, \bar{S}_2, \bar{S}_3]^T \in \boldsymbol{R}^n$ was defined as follows:

$$\overline{\boldsymbol{S}}(\hat{\boldsymbol{x}}_1) = \begin{cases} \left[\text{sign}(\hat{x}_{11})\hat{x}_{11}^2, \text{sign}(\hat{x}_{12})\hat{x}_{12}^2, \text{sign}(\hat{x}_{13})\hat{x}_{13}^2\right]^T & \overline{S}_i \neq 0, |\hat{x}_{1i}| < \varepsilon \\ \left[|\hat{x}_{11}|^{a_0/b_0}\,\text{sign}(\hat{x}_{11}), |\hat{x}_{12}|^{a_0/b_0}\,\text{sign}(\hat{x}_{12}), |\hat{x}_{13}|^{a_0/b_0}\,\text{sign}(\hat{x}_{13})\right]^T & \text{others} \end{cases}$$

where i = 1,2,3, and both a_0 and b_0 are positive odd integers and satisfy $0 < \frac{a_0}{b_0} < 1$.

The differential calculus equation of the fast terminal sliding surface in Equation (8) could be shown as follows:

$$\begin{aligned} \dot{\boldsymbol{S}}_{SMC} &= \dot{\hat{\boldsymbol{x}}}_2 + \boldsymbol{l}_1\dot{\hat{\boldsymbol{x}}}_1 + \boldsymbol{l}_2\boldsymbol{D}_{x_1}\hat{\boldsymbol{x}}_2 \\ &= \boldsymbol{F} + \boldsymbol{G}_1\boldsymbol{E}(t)\boldsymbol{\delta}(t) + \boldsymbol{G}_1\boldsymbol{\rho}(t) + \boldsymbol{D}(t) + \boldsymbol{l}_1\hat{\boldsymbol{x}}_2 + \boldsymbol{l}_2\boldsymbol{D}_{x_1}\hat{\boldsymbol{x}}_2 \\ &= \boldsymbol{F} + \boldsymbol{G}_1\hat{\boldsymbol{E}}(t)\boldsymbol{\delta}(t) + \boldsymbol{G}_1\hat{\boldsymbol{\rho}}(t) + \boldsymbol{l}_1\hat{\boldsymbol{x}}_2 + \boldsymbol{l}_2\boldsymbol{D}_{x_1}\hat{\boldsymbol{x}}_2 + \boldsymbol{\Delta}(t) \end{aligned} \tag{9}$$

where

$$\boldsymbol{D}_{x_1} = \begin{cases} \text{diag}\{2\hat{x}_{1i}\,\text{sign}(\hat{x}_{1i})\} & \bar{S}_i \neq 0,\ |\hat{x}_{1i}| < \varepsilon \\ \dfrac{a_0}{b_0}\,\text{diag}\left\{|\hat{x}_{1i}|^{a_0/b_0-1}\,\text{sign}(\hat{x}_{1i})\right\} & others \end{cases}$$

where $\hat{\boldsymbol{E}}$ and $\hat{\boldsymbol{\rho}}$ are the estimated values of $\boldsymbol{E}$ and $\boldsymbol{\rho}$, respectively, and, i = 1,2,3. In addition, $\boldsymbol{\Delta}(t) = \boldsymbol{G}_1\tilde{\boldsymbol{E}}(t)\boldsymbol{\delta}(t) + \boldsymbol{G}_1\tilde{\boldsymbol{\rho}}(t) + \boldsymbol{D}(t)$ represents uncertainties that could be approximately obtained by the Radical Basis Function Neural Network (RBFNN) [20], where $\tilde{\boldsymbol{E}} \triangleq \boldsymbol{E} - \hat{\boldsymbol{E}}$, $\tilde{\boldsymbol{\rho}} \triangleq \boldsymbol{\rho} - \hat{\boldsymbol{\rho}}$ are the estimation error values. Thus, Equation (9) could be rewritten as follows:

$$\dot{\boldsymbol{S}}_{SMC} = \boldsymbol{F} + \boldsymbol{G}_1\hat{\boldsymbol{E}}(t)\boldsymbol{\delta}(t) + \boldsymbol{G}_1\hat{\boldsymbol{\rho}}(t) + \boldsymbol{l}_1\hat{\boldsymbol{x}}_2 + \boldsymbol{l}_2\boldsymbol{D}_{x_1}\hat{\boldsymbol{x}}_2 + \boldsymbol{W}_1^T\boldsymbol{\phi}_1 + \boldsymbol{\varepsilon}_1 \tag{10}$$

where $\boldsymbol{W}_1$ and $\boldsymbol{\phi}_1$ are the weight matrix and Radical Basis Function, respectively, and $\boldsymbol{\varepsilon}_1$ is approximation error.

2.2.2. Comprehensive Evaluation Index Function (CEIF) Design

According to the dynamic quality indexes in the time response of systems, the controlling effectiveness was evaluated by designing a novel Comprehensive Evaluation Index Function (CEIF) $\boldsymbol{F}$ based on the rise time t_r, the maximum overshoot σ_p, and the transient time t_s.

The expression of the CEIF could be shown as follows:

$$F = \begin{cases} t_r{}^{\frac{1}{t_s}}\sigma_p, & 0 < t_r < 1 \\ t_r{}^{t_s}\sigma_p, & t_r \geq 1 \end{cases} \tag{11}$$

Index One: Rise Time t_r

The time during which a step response curve firstly rises to a steady-state value from 0 was defined as the Rise Time.

Index Two: Maximum Overshoot σ_p

For the maximum value of the step response curse, the Maximum Overshoot was defined as follows:

$$\sigma_p = \frac{|c(t_p) - c(\infty)|}{|c(0) - c(\infty)|} \times 100\%$$

where $c(0)$, $c(t_p)$ and $c(\infty)$ represent the variables of the attitude angles of the launch vehicles in the start-up instant, the overshoot peak instant and the steady-state instant, respectively.

The higher the value of σ_p is, the weaker the System Damping Characteristics are.

Index Three: Transient Time t_s

The time during which the step response curse enters and stays in the allowable error range was defined as the transient time or adjustment time. The above error range was usually Δ times the steady-state value, where Δ is the error band.

The designing principles of the CEIF could be shown as follows:

(1) The CEIF designed in this paper needs to fulfill two purposes: Firstly, the dynamic response speed of the launch vehicle attitude should be guaranteed; Secondly, the dynamic response stability of the launch vehicle attitude should also be ensured. Among the three indexes, the rise time t_r reflects the response speed of the system, the maximum overshoot σ_p represents the operational stability of the system (i.e., the damping degree), and the transient time t_s can concurrently show both the response speed and the damping degree [19]. Therefore, while designing CEIF, all three indexes are considered simultaneously.

(2) After examination, no matter whether the rise time t_r satisfies $0 < t_r < 1$ or $t_r \geq 1$, and no matter whether the transient time t_s satisfies $0 < t_s < 1$ or $t_s \geq 1$, the CEIF is positively correlated with the rise time t_r. Additionally, the positive correlation between the CEIF and the transient time t_s could be shown, and the positive relationship between the CEIF and the maximum overshoot σ_p could also be found. According to the definitions, the shorter the rise time t_r, and with maximum overshoot σ_p or transient time t_s, the better the control property is. therefore, the smaller the CEIF value F is, the better the effectiveness the control's performance.

2.2.3. Sliding Mode Reaching Law Design Resulting in Better Launch Vehicle Attitude Fault-Tolerant Control Performance

The merit of the Constant Reaching Law and that of the Power Reaching Law has been synthesized by designing a Constant Power Reaching Law (CPRL), the expression of which can be shown as follows:

$$\dot{\boldsymbol{S}}_{SMC} = -\boldsymbol{\varepsilon}\,\mathrm{sign}(\boldsymbol{S}_{SMC}) - \boldsymbol{k}_2|\boldsymbol{S}_{SMC}|^{\alpha}\,\mathrm{sign}(\boldsymbol{S}_{SMC}) \tag{12}$$

where $\boldsymbol{\varepsilon} = \mathrm{diag}(\varepsilon_1, \varepsilon_2, \varepsilon_3), \varepsilon_i > 0$, $i = 1,2,3$, $0 < \alpha < 1$, $\boldsymbol{k}_2 = \mathrm{diag}(k_{21}, k_{22}, k_{23})$, $k_{21} > 0, k_{22} > 0, k_{23} > 0$, $\mathrm{sign}(\boldsymbol{S}_{SMC}) = [\mathrm{sign}(S_{SMC(1)}), \mathrm{sign}(S_{SMC(2)}), \mathrm{sign}(S_{SMC(3)})]^T$, $|\boldsymbol{S}_{SMC}|^{\alpha}\ \mathrm{sign}(\boldsymbol{S}_{SMC}) = [|S_{SMC(1)}|^{\alpha}\,\mathrm{sign}(S_{SMC(1)}), |S_{SMC(2)}|^{\alpha}\,\mathrm{sign}(S_{SMC(2)}), |S_{SMC(3)}|^{\alpha}\,\mathrm{sign}(S_{SMC(3)})]^T$.

In the revelation of the surface expression of the fast terminal sliding mode represented by Equation (8), the closer the absolute values of $\hat{\boldsymbol{x}}_1$ and $\hat{\boldsymbol{x}}_2$ are to zero, the closer the value of $|\boldsymbol{S}_{SMC}|$ to zero. Hence, the convergence process of $\hat{\boldsymbol{x}}_1$ and $\hat{\boldsymbol{x}}_2$ in the fast terminal sliding mode control is also the convergence process of $\boldsymbol{S}_{SMC}$.

The design principles of the new reaching law are as follows:

(1) To guarantee that the phase trajectory converges towards the origin of the phase plane as time progresses in the fast terminal sliding mode control, the phase trajectory of a single attitude channel should pass through the origin and be located in the second and fourth quadrants of the phase plane. Its schematic diagram is shown in Figure 3. Therefore, all the terms on the right side of the equal sign in the reaching law expression represented by Equation (12) are negative.

(2) The Phase Trajectory Diagram of the Reaching Law of the ith Attitude Channel is reflected in Figure 3; the red box contains the region where the absolute value of the change in $\frac{dS_{\mathrm{SMC}(i)}}{dt}$ $(i = 1,2,3)$ decreases sharply as the absolute value of $S_{\mathrm{SMC}(i)}$ $(i = 1,2,3)$ decreases; the green box contains the region where the absolute value of the change in $\frac{dS_{\mathrm{SMC}(i)}}{dt}$ remains high as the absolute value of $S_{\mathrm{SMC}(i)}$ decreases.

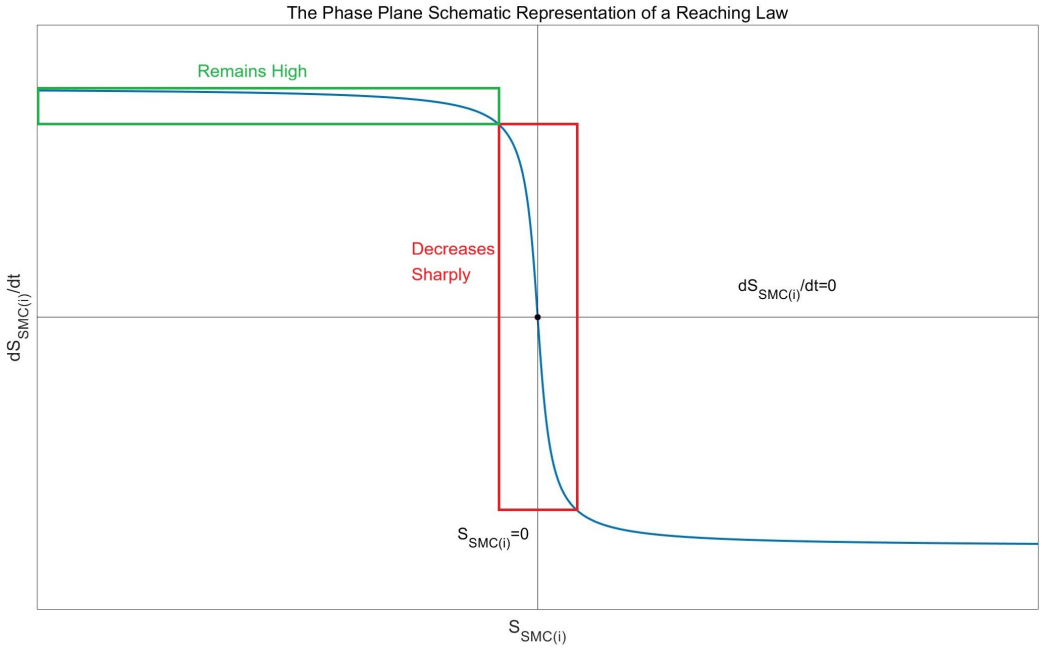


Figure 3. ThePhase trajectory diagram of the Reaching Law of the *i*th Attitude Channel.

(3) The sign-function-related term of the Constant Reaching Law can ensure that the system state in the vicinity of the origin of the phase plane approaches the origin with a sufficiently large $\left|\dot{S}_{SMC(i)}\right|$ value (i.e., maintaining a sufficiently large rate of change of $\left|S_{SMC(i)}\right|$), while $\left|S_{SMC(i)}\right|$ is determined by the difference between the system state and the expected value of the system state (which is the stable value of the system state after a fault occurs). In view of this, compared with the reaching laws without the term related to the sign function in the Constant Reaching Law, including the Power Reaching Law, first, the term related to the sign function in the Constant Reaching Law can ensure that the dynamic response speed of the launch vehicle attitude towards the expected value is faster when the distance to the expected value is closer; that is, the rise time t_r is shorter. Second, as mentioned above, once the system state value crosses the origin of the phase plane, $\left|\dot{S}_{SMC(i)}\right|$ would be assigned the opposite sign to $\left|S_{SMC(i)}\right|$. Therefore, if the $\left|\dot{S}_{SMC(i)}\right|$ value is better guaranteed, it will more effectively prevent the system state from deviating from the origin of the phase plane, and the dynamic response stability of the launch vehicle attitude can also be guaranteed; that is, the maximum overshoot (quantity) σ_p is smaller than that of the reaching law without the term related to the sign function in the Constant Reaching Law. Thus, the comprehensive evaluation index function F will likely be smaller accordingly.

(4) As the exponent of the term related to the power function in the Power Reaching Law is $0 < \alpha < 1$, when $S_{SMC(i)} < 0$, $\dot{S}_{SMC(i)} = -k_{2i}\left|S_{SMC(i)}\right|^{\alpha} \mathrm{sign}(S_{SMC(i)})$ exhibits an upward convex shape in the second quadrant of the phase plane. When $S_{SMC(i)} > 0$, it presents a downward convex shape in the fourth quadrant. Based on the above patterns, when the state function starts from the same initial point in the phase plane and the value of $\left|S_{SMC(i)}\right|$ gradually decreases, the term related to the power function in the Power Reaching Law causes the value of $\left|\dot{S}_{SMC(i)}\right|$ to decrease from slowly to rapidly. Compared with the uniform decrease in the $\left|\dot{S}_{SMC(i)}\right|$ value of mathematical terms such as $-k_{1i}S_{SMC(i)}$ including the exponential reaching law, the term related to the power function in the Power Reaching Law can ensure that the system state still approaches the origin of the phase plane with a relatively larger $\left|\dot{S}_{SMC(i)}\right|$ value in the vicinity of its origin. Similar to the principle of (2),

under the premise of the same other conditions, the term related to the power function in the Power Reaching Law can guarantee that the dynamic response rise time t_r of the launch vehicle attitude is shorter than the rise time of mathematical terms such as $-k_{1i}S_{SMC(i)}$ of reaching laws like the exponential reaching law and the maximum overshoot (quantity) σ_p is smaller than the maximum overshoot (quantity) σ_p of mathematical terms such as $-k_{1i}S_{SMC(i)}$ of the exponential reaching law. Thus, the comprehensive evaluation index function F is likely to be smaller accordingly.

(5) To superimpose the aforementioned advantages of the Constant Reaching Law on those of the Power Reaching Law, the CPRL expression designed in this paper incorporates both the term related to the sign function in the Constant Reaching Law and the term related to the power function in the Power Reaching Law.

2.2.4. Fault-Tolerant Control Law Design

Considering system (7), the fault-tolerant control law has been designed as

$$\boldsymbol{u} = \boldsymbol{\delta}(t) = -\hat{\boldsymbol{E}}^2\boldsymbol{G}_1^T\left[\boldsymbol{G}_1\hat{\boldsymbol{E}}^3\boldsymbol{G}_1^T\right]^{-1}(\boldsymbol{\delta}_1 + \boldsymbol{\delta}_2) \tag{13}$$

where $\boldsymbol{\delta}_1 = \frac{\boldsymbol{S}}{\|\boldsymbol{S}\|+\zeta}\left(\|\boldsymbol{F} + \boldsymbol{l}_1\hat{\boldsymbol{x}}_2 + \boldsymbol{l}_2\boldsymbol{D}_{x_1}\hat{\boldsymbol{x}}_2 + \boldsymbol{G}_1\hat{\boldsymbol{\rho}}\| + \left\|\hat{\boldsymbol{W}}_1^T\boldsymbol{\phi}_1\right\| + \|\hat{\boldsymbol{\varepsilon}}_1\|\right)$, $\boldsymbol{\delta}_2 = -\dot{\boldsymbol{S}}_{SMC} = \boldsymbol{\varepsilon}$ $\text{sign}(\boldsymbol{S}_{SMC}) + \boldsymbol{k}_2|\boldsymbol{S}_{SMC}|^{\alpha}\,\text{sign}(\boldsymbol{S}_{SMC})$, and the adaptive updating law of the parameters in the neural network was $\dot{\hat{\boldsymbol{W}}}_1 = -\frac{1}{\gamma}\boldsymbol{\phi}_1\boldsymbol{S}_{SMC}^T$, where $\hat{\boldsymbol{W}}_1$ and $\hat{\boldsymbol{\varepsilon}}_1$ are the estimated values of $\boldsymbol{W}_1$ and $\boldsymbol{\varepsilon}_1$, respectively.

Note: In the design of the fault-tolerant control law, a Radial Basis Function Neural Network (RBFNN) is adopted to handle the uncertainties in the sliding mode dynamics [20].

3. Results and Discussion

3.1. Experimental Tools

MATLAB R2023b was used to carry out the design, test and verification of the launch vehicle attitude control close-loop. This simulation software has shown its functions of efficient numerical calculation and symbolic calculation to finish the time iteration swiftly; at the same time, its complete graphic processing function has realized visualization of calculation results and computer programming, being convenient for the intuitive comparison among the launch vehicle attitude values influenced by different reaching laws.

For the above reasons, while establishing the launch vehicle model and designing the launch vehicle attitude control laws, this paper fully applied the functions of the MATLAB Function in the MATLAB, writing the m function of MATLAB in the Simulink models. At once, since many different reaching laws has been applied in the launch vehicle attitude fault-tolerant laws as members of the experimental group or control group, in order to test and verify the effect of the CEIF constructed in this paper and compare the effects of evaluation of these control laws, a series of functions in the m file of MATLAB R2023b was utilized for simulation.

3.2. Experimental Results Analyses

This section focuses on the verification of the CEIF and launch vehicle attitude fault-tolerant controller designed above to prove their effectiveness. The simulation model was established mainly by consultingthe literature [20,21]. The moment of inertia was $\boldsymbol{J} = \text{diag}\left\{2.9 \times 10^6\ \text{kg}\cdot\text{m}^2,\ 5.9 \times 10^7\ \text{kg}\cdot\text{m}^2,\ 5.9 \times 10^7\ \text{kg}\cdot\text{m}^2\right\}$, the initial value of the launch vehicle attitude control system was $\boldsymbol{\xi} = [\varphi, \psi, \theta]^T = [0°, 0°, 90°]^T$, $\boldsymbol{\omega} = \left[\omega_x, \omega_y, \omega_z\right]^T = [0, 0, 0]^T(°)\cdot s^{-1}$, the attitude instruction signal was

$\xi_c = [-10°, 15°, 80°]^T$. At the same time, this simulation has considered the influence of the external disturbance $\boldsymbol{d} = 0.05 \cdot [\sin(t), \cos(2t), \sin(3t)]^T N \cdot m$ on the launch vehicle attitude control system.

As shown in Table 1, in the controller, eight reaching laws were adopted to perform the simulation and compare the control results. In them, Reaching Law One, Reaching Law Two and Reaching Law Three represented the Constant Reaching Law, Exponential Reaching Law and the Power Reaching Law, respectively; Reaching Law Six adopted the Constant Power Reaching Law (CPRL) designed in this paper; all the rest of the reaching laws played the role of control group members.

When the parameters of the sliding mode reaching laws were $a = 5$, $b = 7$, $\boldsymbol{k}_1 = \mathrm{diag}\{5,5,5\}$, $\boldsymbol{k}_2 = \mathrm{diag}\{25,25,25\}$, $\boldsymbol{\varepsilon} = \mathrm{diag}\{3,3,3\}$, $a_a = 6$, the parameters of the failure about the loss of effectiveness were $E_1 = 0.3$, $E_2 = 0.2$, the parameters of the failure about deviation were $\rho_1 = 0.6$, $\rho_2 = 0.5$, and the parameters of the terminal sliding face were $l_1 = \mathrm{diag}\{1,1,2\}$, $l_2 = \mathrm{diag}\{1,1,2\}$. The absolute values of the differences between the peak values of the attitude angles in three channels after failures and the objective values of the attitude angles in the three channels could are shown in Table 2.

Table 1. Comparison table of the reaching laws adopted in this paper.

Reference Numbers of Reaching Laws	Names of Reaching Laws	Expressions of Reaching Laws
Reaching Law One	Constant Reaching Law	$\dot{\boldsymbol{S}}_{SMC} = -\boldsymbol{\varepsilon}\,\mathrm{sign}(\boldsymbol{S}_{SMC})$
Reaching Law Two	Exponential Reaching Law	$\dot{\boldsymbol{S}}_{SMC} = -\boldsymbol{\varepsilon}\,\mathrm{sign}(\boldsymbol{S}_{SMC}) - \boldsymbol{k}_1\boldsymbol{S}_{SMC}$
Reaching Law Three	Power Reaching Law	$\dot{\boldsymbol{S}}_{SMC} = -\boldsymbol{k}_2\lvert\boldsymbol{S}_{SMC}\rvert^{\alpha}\,\mathrm{sign}(\boldsymbol{S}_{SMC})$
Reaching Law Four	Regular Reaching Law	$\dot{\boldsymbol{S}}_{SMC} = -\boldsymbol{\varepsilon}\,\mathrm{sign}(\boldsymbol{S}_{SMC}) - a_a f(\boldsymbol{S}_{SMC})$
Reaching Law Five	Compound Reaching Law One	$\dot{\boldsymbol{S}}_{SMC} = -\boldsymbol{k}_1\boldsymbol{S}_{SMC} - \boldsymbol{k}_2\lvert\boldsymbol{S}_{SMC}\rvert^{\alpha}\,\mathrm{sign}(\boldsymbol{S}_{SMC})$
Reaching Law Six	Compound Reaching Law Two (CPRL)	$\dot{\boldsymbol{S}}_{SMC} = -\boldsymbol{\varepsilon}\,\mathrm{sign}(\boldsymbol{S}_{SMC}) - \boldsymbol{k}_2\lvert\boldsymbol{S}_{SMC}\rvert^{\alpha}\,\mathrm{sign}(\boldsymbol{S}_{SMC})$
Reaching Law Seven	Compound Reaching Law Three	$\dot{\boldsymbol{S}}_{SMC} = -\boldsymbol{k}_2\lvert\boldsymbol{S}_{SMC}\rvert^{\alpha}\,\mathrm{sign}(\boldsymbol{S}_{SMC}) - a_a f(\boldsymbol{S}_{SMC})$
Reaching Law Eight	Compound Reaching Law Four	$\dot{\boldsymbol{S}}_{SMC} = -a_a f(\boldsymbol{S}_{SMC}) - \boldsymbol{k}_1\boldsymbol{S}_{SMC}$

where $\boldsymbol{\varepsilon} = \mathrm{diag}\{\varepsilon_1, \varepsilon_2, \varepsilon_3\}, \varepsilon_i > 0, i = 1,2,3$, $\boldsymbol{S}_{SMC} = \left[S_{SMC(1)}, S_{SMC(2)}, S_{SMC(3)}\right]^T$,
$\mathrm{sign}(\boldsymbol{S}_{SMC}) = [\mathrm{sign}(S_{SMC(1)}), \mathrm{sign}(S_{SMC(2)}), \mathrm{sign}(S_{SMC(3)})]^T$,
$\lvert\boldsymbol{S}_{SMC}\rvert^{\alpha}\,\mathrm{sign}(\boldsymbol{S}_{SMC}) = \left[\left|S_{SMC(1)}\right|^{\alpha}\mathrm{sign}(S_{SMC(1)}), \left|S_{SMC(2)}\right|^{\alpha}\mathrm{sign}(S_{SMC(2)}), \left|S_{SMC(3)}\right|^{\alpha}\mathrm{sign}(S_{SMC(3)})\right]^T, 0 < \alpha < 1$,
$\boldsymbol{k}_1 = \mathrm{diag}\{k_{11}, k_{12}, k_{13}\}, k_{11} > 0, k_{12} > 0, k_{13} > 0, \boldsymbol{k}_2 = \mathrm{diag}\{k_{21}, k_{22}, k_{23}\}, k_{21} > 0, k_{22} > 0, k_{23} > 0, a_a > 0$,
$f(\boldsymbol{S}_{SMC}) = \left[f\left(S_{SMC(1)}\right), f\left(S_{SMC(2)}\right), f\left(S_{SMC(3)}\right)\right]^T, f\left(S_{SMC(i)}\right) = S_{SMC(i)} - \sin\left(S_{SMC(i)}\right), i = 1,2,3$

According to the Min-1 normalization of population variance, the differences among the influence of the different reaching laws on the pitching angles in the pitching channel comprehensive faults were much smaller than the differences among the influence of the different reaching laws on the rolling angles in the rolling channel comprehensive faults. Similarly, the differences among the influence of the different reaching laws on the yawing angles in the yawing channel comprehensive faults were much smaller than the differences among the influence of the different reaching laws on the rolling angles in the rolling channel comprehensive faults. Based on the above consideration, each failure was placed in the rolling channel in this paper. When the parameters of the slide mode reaching laws remained constant, by separately observing the rolling channel, the phase trajectories of the different reaching laws could be shown in Figure 4.

Table 2. Comparison table of the absolute values of differences between the peak values of the attitude angles in three channels after failures and the objective values of the attitude angles in three channels.

	The Absolute Values of Differences Between Two Values *		
	Pitching Channel	**Yawing Channel**	**Rolling Channel**
Reaching Law One	0.0020	0.0044	0.0816
Reaching Law Two	0.0019	0.0051	0.0756
Reaching Law Three	0.0055	0.0155	0.1528
Reaching Law Four	0.0022	0.0053	0.0829
Reaching Law Five	0.0051	0.0143	0.1405
Reaching Law Six	0.0017	0.0068	0.0322
Reaching Law Seven	0.0055	0.0155	0.1528
Reaching Law Eight	0.1204	0.5299	1.7765
The Population Variance of the Absolute Values **	2.954×10^{-6}	2.353×10^{-5}	1.856×10^{-3}
Min-1 normalization of population variance	1	7.965	628.2

* The two values indicate the Peak Value of the Attitude Angles in a Certain Channel after Failures and the Objective Value of the Attitude Angles in that Chaninenel; ** The Absolute values associated with Reaching Law Eight are much larger than the remaining values and are therefore excluded from the computation.

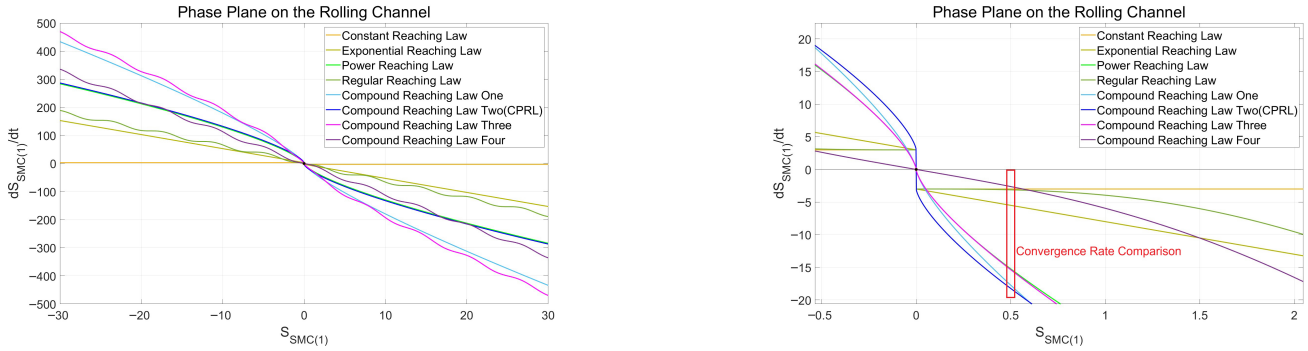


Figure 4. The phase trajectories graph of the different reaching laws in the rolling channel. (**a**) The original graph of the phase trajectories. (**b**) The enlarged partial graph of the phase plane in a small horizontal coordinate range.

Figure 4a shows the phase trajectories of the eight reaching laws. In the process of the sliding mode control, the phase trajectories gradually approached to the coordinate origin as time passed, known in the information in the enlarged partial graph in Figure 4b, when the absolute values of the phase plane horizontal coordinate $S_{SMC(1)}$ entered a small range, which means sliding through the area contained by the red box in Figure 4b from the area far from the original point of the phase plane. This effect was especially pronounced after this horizontal coordinate was smaller than 0.5, thanks to the term related to the sign function in the Constant Reaching Law $-\boldsymbol{\varepsilon}\,\mathrm{sign}(\boldsymbol{S}_{SMC})$ in Reaching Law Six designed in this paper. The absolute value of the vertical coordinate $\dot{S}_{SMC(1)}$ of Reaching Law Six was obviously larger than the absolute values of the vertical coordinate $\dot{S}_{SMC(1)}$ of Reaching Law Three, Reaching Law Five, Reaching Law Seven, and Reaching Law Eight without the term related to the sign function in the Constant Reaching Law $-\boldsymbol{\varepsilon}\,\mathrm{sign}(\boldsymbol{S}_{SMC})$. Even if there similarly existed the term related to the sign function in the Constant Reaching Law $-\boldsymbol{\varepsilon}\,\mathrm{sign}(\boldsymbol{S}_{SMC})$, the term related to the power function in the Power Reaching Law $-\boldsymbol{k}_2|\boldsymbol{S}_{SMC}|^{\alpha}\,\mathrm{sign}(\boldsymbol{S}_{SMC})$ of Reaching Law Six still assisted the absolute value of its vertical coordinate $\dot{S}_{SMC(1)}$ of Reaching Law Six, being obviously larger than the absolute values of those of Reaching Law One, Reaching Law Two and Reaching Law Four. Therefore, when the horizontal coordinate of the phase plane was small enough, Reaching Law Six could approach to the coordinate origin with the fastest speed, i.e, the rise time of Reaching

Law Six was the shortest; in the real control, the control system usually appeared as the maximum overshoot (quantity) σ_p. This, in the phase plane, could be expressed as the phase trajectory continuing to enter the other side of the coordinate origin after it arrived at this coordinate origin. After this occurred, the phase trajectory could return to the coordinate origin with the largest negative increment with the help of Reaching Law Six, i.e, the maximum overshoot (quantity) σ_p of Reaching Law Six was the smallest.

It was assumed that the faults expressed in Equation (14) occurred in the simulation of launch vehicle swinging actuators. In detail, the faults were defined to occur when the time of t_f came, which could be shown as follows:

$$\boldsymbol{E} = \begin{cases} \mathrm{diag}\{1,1,1\}, & 0 \le t < t_f \\ \mathrm{diag}\{\left[E_1 + E_2 \sin\left(0.5t + \frac{2\pi}{3}\right)\right], 1, 1\}, & t \ge t_f \end{cases} \quad \boldsymbol{\rho} = \begin{cases} [0,0,0]^T, & 0 \le t < t_f \\ [\rho_1 + \rho_2 \sin(0.2\pi t), 0, 0]^T, & t \ge t_f \end{cases} \tag{14}$$

In the current experiments, the parameters of the failure regarding the loss of effectiveness, the parameters of the failure regarding deviation, the parameters of the terminal sliding face, and the parameters of the slide mode reaching laws are consistent with those parameters mentioned above, setting the moment of fault occurring to 2 s. Known in Equation (14), both the failure regarding the loss of effectiveness and the failure regarding deviation occurred in the rolling channel of actuators in the simulation at 2 s, shown in Figure 5.

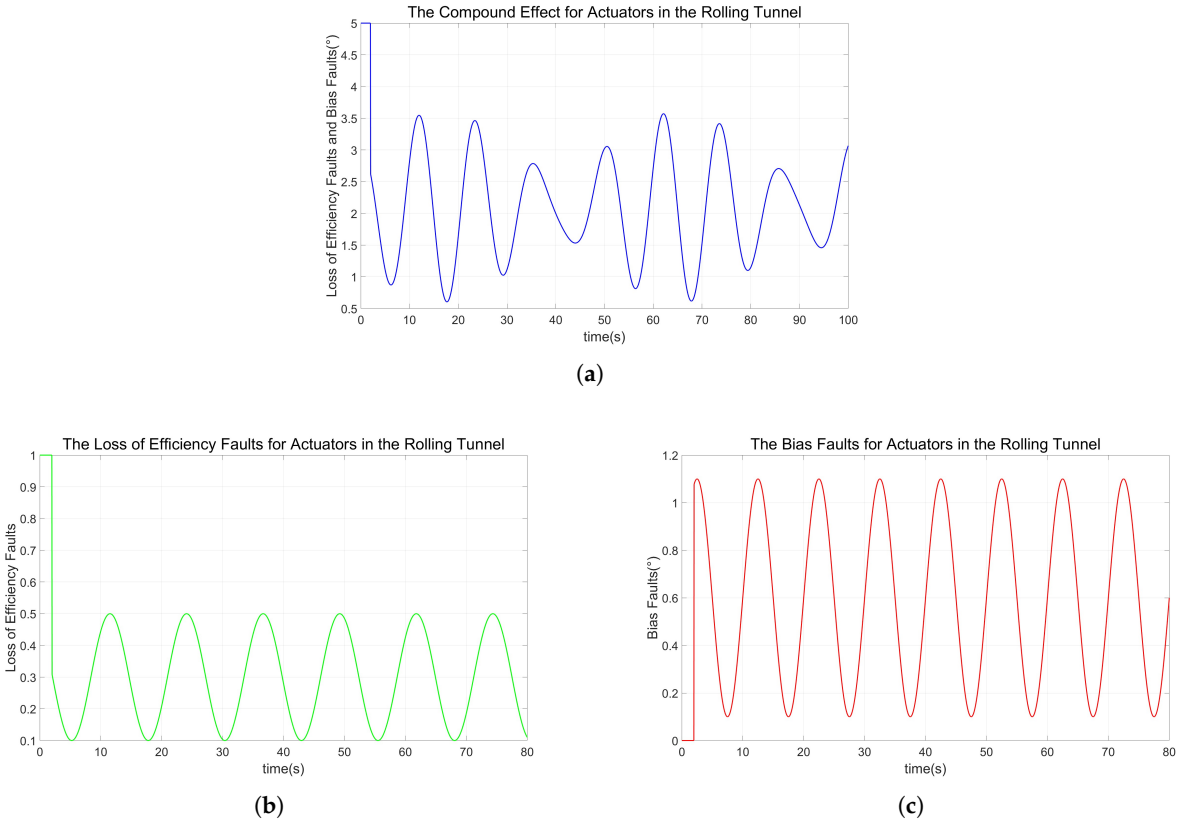


Figure 5. Sketch graphs of the actuator failures in the rolling channel. (**a**) The compound effect of loss of efficiency faults and the bias faults for actuators in the rolling tunnel (assuming that the control input δ_x for the rolling channel is constant at 5 degrees). (**b**) The sketch graph of the actuator failure about the loss of effectiveness in the rolling channel. (**c**) The sketch graph of the actuator failure regarding deviation in the rolling channel.

Before and after the above faults occurred, some of the function indexes—used in calculating the CEIF in Equation (11)—and the final calculation results of the CEIF were all arranged in ascending order of their values shown in Table 3.

Table 3. Comparison table of some function indexes used to calculate the CEIF and the final calculation results.

Compared Indexes	Comparison Results	
	Before Failures Occurred	**After Failures Occurred**
Rise Time t_r	$t_{r16} < t_{r15} < t_{r13} < t_{r17} < t_{r12} < t_{r14} < t_{r18} < t_{r11}$	$t_{r26} < t_{r24} < t_{r21} < t_{r22} < t_{r23} < t_{r27} < t_{r25} < t_{r28}$
Maximum Overshoot σ_p	$\sigma_{p16} < \sigma_{p13} < \sigma_{p15} < \sigma_{p17} < \sigma_{p11} < \sigma_{p14} < \sigma_{p12} < \sigma_{p18}$	$\sigma_{p26} < \sigma_{p22} < \sigma_{p24} < \sigma_{p21} < \sigma_{p28} < \sigma_{p25} < \sigma_{p27} < \sigma_{p23}$
CEIF F	$F_{16} < F_{15} < F_{13} < F_{17} < F_{11} < F_{14} < F_{12} < F_{18}$	$F_{26} < F_{22} < F_{24} < F_{21} < F_{27} < F_{23} < F_{25} < F_{28}$

The following information is reflected in Table 3:

(1) Before the failures occurred, the rise time t_{r12} of the Exponential Reaching Law was shorter than the rise time t_{r11} of the Constant Reaching Law, but the maximum overshoot σ_{p12} of the Exponential Reaching Law was larger than the maximum overshoot σ_{p11} of the Constant Reaching Law. On the contrary, after the failures occurred, the rise time t_{r22} of the Exponential Reaching Law was longer than the rise time t_{r21} of the Constant Reaching Law, but the maximum overshoot σ_{p22} of the Exponential Reaching Law was smaller than the maximum overshoot σ_{p21} of the Constant Reaching Law. In addition, after the failures occurred, the rise time t_{r23} of the Power Reaching Law was longer than not only t_{r21} but also t_{r22}, and the maximum overshoot σ_{p23} of the Power Reaching Law was larger than not only σ_{p21} but also σ_{p22}. Since the rise time could reflect the characters of the response speed of a system and the maximum overshoot could reflect the characters of the operation stability of that system, the above comparison results illustrated that the difficulty in coordinating the response speed of the attitude angles with the operation stability of these angles frequently arose.

(2) Before the failures occurred, the rise time t_{r13} of the Power Reaching Law was obviously shorter than both the rise time t_{r11} of the Constant Reaching Law and the rise time t_{r12} of the Exponential Reaching Law. The maximum overshoot σ_{p13} of the Power Reaching Law was smaller than both the maximum overshoot σ_{p11} of the Constant Reaching Law and the maximum overshoot σ_{p12} of the Exponential Reaching Law. At this time, the CEIF F_{13} of the Power Reaching Law was smaller than both the CEIF F_{11} of the Constant Reaching Law and the CEIF F_{12} of the Exponential Reaching Law. After the failures occurred, both the rise time t_{r21} of the Constant Reaching Law and the rise time t_{r22} of the Exponential Reaching Law were obviously shorter than the rise time t_{r23} of the Power Reaching Law, and both the maximum overshoot σ_{p21} of the Constant Reaching Law and the maximum overshoot σ_{p22} of the Exponential Reaching Law were also smaller than the maximum overshoot σ_{p23} of the Power Reaching Law. At this time, both the CEIF F_{21} of the Constant Reaching Law and the CEIF F_{22} of the Exponential Reaching Law were smaller than the CEIF F_{23} of the Power Reaching Law. Seen in (1), the rise time could reflect the characters of the response speed of a system, and the maximum overshoot could reflect the characters of the operation stability of that system. Thus, the value of CEIF could reflect the levels of both the response speed and the operation stability of a system.

(3) According to the above conclusions, as shown Table 3, before the failures occurred, among the various indexes of the dynamic process of the launch vehicle rolling angle

tracking target rolling angle, the rise time t_{r16} influenced by the CPRL designed in this paper was shorter than the rise time t_{r11} influenced by the Constant Reaching Law, the rise time t_{r12} influenced by the Exponential Reaching Law, and the rise time t_{r13} influenced by Power Reaching Law. The maximum overshoot σ_{p16} influenced by the CPRL designed in this paper was smaller than the maximum overshoot σ_{p11} influenced by the Constant Reaching Law, the maximum overshoot σ_{p12} influenced by the Exponential Reaching Law, and the maximum overshoot σ_{p13} influenced by the Power Reaching Law. The value of CEIF F_{16} influenced by the CPRL designed in this paper was smaller than the value of CEIF F_{11} influenced by the Constant Reaching Law, the value of CEIF F_{12} influenced by the Exponential Reaching Law and the value of CEIF F_{13} influenced by the Power Reaching Law.

(4) After failures occurred, among the various indexes of the dynamic process of the launch vehicle rolling angle deviation value regressing to the stable value again, the rise time t_{r26} influenced by the CPRL designed in this paper was shorter than the rise time t_{r21} influenced by the Constant Reaching Law, the rise time t_{r22} influenced by the Exponential Reaching Law and the rise time t_{r23} influenced by the Power Reaching Law. The maximum overshoot σ_{p26} influenced by the CPRL designed in this paper was smaller than the maximum overshoot σ_{p21} influenced by the Constant Reaching Law, the maximum overshoot σ_{p22} influenced by the Exponential Reaching Law and the maximum overshoot σ_{p23} influenced by the Power Reaching Law. The value of CEIF F_{26} influenced by the CPRL designed in this paper was smaller than the value of CEIF F_{21} influenced by the Constant Reaching Law, the value of CEIF F_{22} influenced by the Exponential Reaching Law and the value of CEIF F_{23} influenced by the Power Reaching Law.

(5) The CEIF represented that in certain conditions—not only before the failures occurred but also after they occurred—the control performance of the control system influenced by the CPRL designed in this paper was the best.

The CEIF values arranged in Table 3 could be calculated and shown in Table 4.

Table 4. CEIF values before and after failures.

Before Failures Occurred		**After Failures Occurred**	
CEIF Arranged in Ascending Order	**Value of the CEIF**	**CEIF Arranged in Ascending Order**	**Value of the CEIF**
F_{16}	9.01×10^{-7}	F_{26}	2.19×10^{5}
F_{15}	1.12×10^{-4}	F_{22}	3.35×10^{5}
F_{13}	1.31×10^{-4}	F_{24}	3.61×10^{5}
F_{17}	1.15×10^{-4}	F_{21}	1.98×10^{6}
F_{11}	0.0020	F_{27}	8.88×10^{7}
F_{14}	0.0022	F_{23}	8.89×10^{7}
F_{12}	0.0034	F_{25}	8.96×10^{7}
F_{18}	0.3062	F_{28}	1.03×10^{9}
The optimal CEIF value drops heavily to 0.81% of the suboptimal one.		The optimal CEIF value drops obviously to 65.45% of the suboptimal one.	

Values are sorted in ascending order of CEIF.

Figure 6 shows the curve of the launch vehicle rolling angle instruction tracking of the launch vehicle attitude system. In these graphs, it is shown that:

(1) All of the launch vehicle attitude angles controlled by the fault-tolerant control laws applying eight reaching laws, respectively, could track to the value of the instruction signal at about 1 second after tracking, shown in Figure 6.

(2) Two seconds after the start of the simulation, the launch vehicle system started to experience actuator failures, shown in Figure 6. The tracking character of the launch vehicle

attitude was clearly affected, and this launch vehicle attitude system showed apparent tracking errors, but employing the eight fault-tolerant control laws, respectively, applying eight reaching laws could lessen the lasting effect of failures on the launch vehicle attitude.

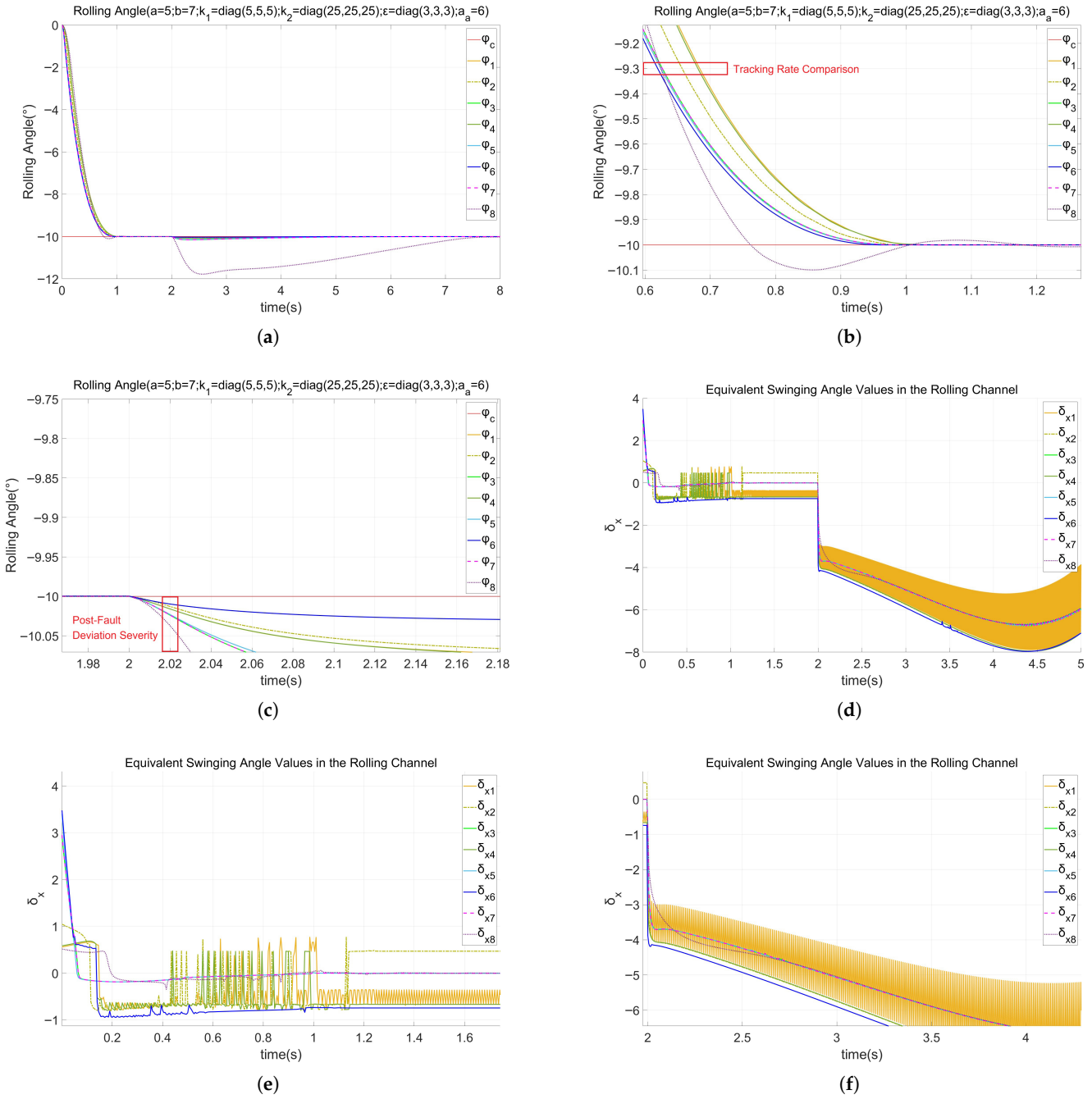


Figure 6. The rolling angle of the launch vehicle considering the failures that occurred and the related equivalent swinging angle values in the rolling channel. (**a**) The original simulation graph of the launch vehicle rolling angle. (**b**) The enlarged partial graph of the launch vehicle rolling angle tracking near the launch vehicle rolling angle tracking-instruction before failures occurred. (**c**) The enlarged partial graph of the launch vehicle rolling angle deviating from the launch vehicle rolling angle tracking-instruction after failures occurred. (**d**) The original simulation graph of the equivalent swinging angle values in the rolling channel. (**e**) The enlarged partial graph of the equivalent swinging angle values of the launch vehicle in the rolling channel before failures occurred. (**f**) The enlarged partial graph of the equivalent swinging angle values of the launch vehicle in the rolling channel after failures occurred.

(3) While the fault-tolerant control laws applying all of these reaching laws—except for the CPRL designed in this paper (Reaching Law Six)—could still accomplish the tracking of the attitude instruction over time, before the failures occurred, employing the fault-tolerant control law applyingthe CPRL designed in this paper could cause the launch vehicle rolling angle value to reach to the tracking-instruction angle value more swiftly and more evenly than the seven control laws respectively applying the rest seven reaching laws, shown in the area contained by the red box in Figure 6b. After the failures occurred, the launch vehicle rolling angles respectively controlled by those seven fault-tolerant control laws applying the rest of the seven reaching laws showed a more severe deviation from the tracking-instruction value than that fault-tolerant control law applying the CPRL designed in this paper, shown in the area contained by the red box in Figure 6c. Therefore, the calculation results of the CEIF were consistent with the laws of comparison obtained by directly observing the launch vehicle rolling angle dynamic variation curves influenced by the eight reaching laws.

(4) Figure 6d–f represent the equivalent swinging angle values influenced by the fault-tolerant control law with the the Constant Power Reaching Law (CPRL, Reaching Law Six), steadily showing the larger absolute value, which means that the fault-tolerant control law with CPRL could offer stronger controlling ability to restrain the deviation from the target value with more swiftness and a smaller overshoot.

The parameters of the failure about the loss of effectiveness are defined as $E_1 = 0.2$, $E_2 = 0.1$, the parameters of the failure regarding deviation were $\rho_1 = 0.6$, $\rho_2 = 0.5$, which means that the parameters of the Loss of Effectiveness became worse and the parameters of the loss of effectiveness remained unchanged. The simulation results of the rolling angle of the launch vehicle are shown in Figure 7a–c.

From Figure 7, even though the parameters of the loss of effectiveness became worse, before the failures occurred, employing the fault-tolerant control law applying the CPRL designed in this paper could cause the launch vehicle rolling angle value to reach the tracking-instruction angle value more swiftly and more evenly than the seven control laws respectively applying the rest of the seven reaching laws after the failures occurred, shown in the areas contained by the red boxes in Figure 7b,c. The launch vehicle rolling angles respectively controlled by those seven fault-tolerant control laws applying the rest of the seven reaching laws still showed more severe deviation from the tracking-instruction value than the fault-tolerant control law applying CPRL.

The parameters of the failure regarding the loss of effectiveness are defined as $E_1 = 0.3$, $E_2 = 0.2$, and the parameters of the failure regarding deviation were $\rho_1 = 0.7$, $\rho_2 = 0.6$, which means that the parameters of the failure regarding deviation became worse and the parameters of the loss of effectiveness remained unchanged. The simulation results of the rolling angle of the launch vehicle are shown in Figure 8a–c.

From Figure 8, even though the parameters of the failure regarding deviation became worse, before the failures occurred, employing the fault-tolerant control law applying the CPRL designed in this paper could cause the launch vehicle rolling angle value to reach to the tracking-instruction angle value more swiftly and more evenly than the seven control laws respectively applying the rest of the seven reaching laws after the failures occurred, shown in the areas contained by the red boxes in Figure 8b,c. The launch vehicle rolling angles respectively controlled by those seven fault-tolerant control laws applying the rest of the seven reaching laws still showed the most severe deviation from the tracking-instruction value compared to the fault-tolerant control law applying CPRL.

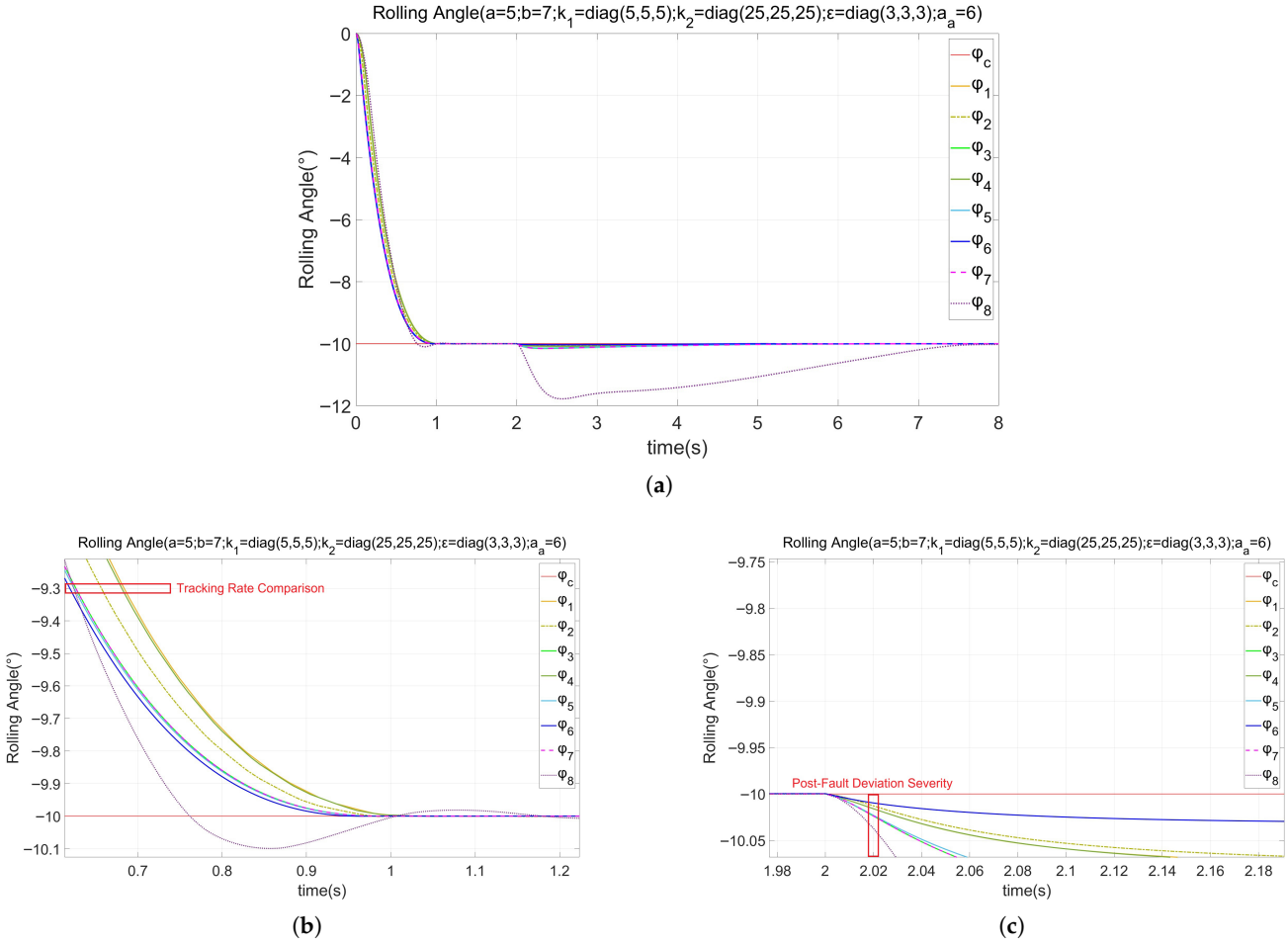


Figure 7. Enlarged partial graph of the launch vehicle rolling angle deviating from the launch vehicle rolling angle tracking-instruction when the parameters of the loss of effectiveness became worse. (**a**) The original simulation graph of the launch vehicle rolling angle. (**b**) The enlarged partial graph of the launch vehicle rolling angle tracking near the launch vehicle rolling angle tracking-instruction before failures occurred. (**c**) The enlarged partial graph of the launch vehicle rolling angle deviating from the launch vehicle rolling angle tracking-instruction after failures occurred.

In Table 5, the Two Power Reaching Law was proposed by Mei H. et al. [17] and used by Zhang H. X. [13]; the Multi Power Reaching Law was proposed by Zhang Y. et al. [18].

Table 5. Comparison table of the CPRL, Two Power Reaching Law and Multi Power Reaching Law.

Reference Numbers	Names	Expressions
Reaching Law Six	Constant Power Reaching Law (CPRL)	$\dot{S}_{SMC} = -\varepsilon \operatorname{sign}(S_{SMC}) - k_2 \lvert S_{SMC}\rvert^{\alpha} \operatorname{sign}(S_{SMC})$
Reaching Law Nine	Two Power Reaching Law	$\dot{S}_{SMC} = -k_2 \lvert S_{SMC}\rvert^{\alpha} \operatorname{sign}(S_{SMC}) - k_3 \lvert S_{SMC}\rvert^{\alpha_2} \operatorname{sign}(S_{SMC})$
Reaching Law Ten	Multi-Power Reaching Law	$\dot{S}_{SMC} = -k_1 S_{SMC} - k_2 \lvert S_{SMC}\rvert^{\alpha} \operatorname{sign}(S_{SMC}) - k_3 \lvert S_{SMC}\rvert^{\alpha_2} \operatorname{sign}(S_{SMC}) - k_4 \lvert S_{SMC}\rvert^{\alpha_3} \operatorname{sign}(S_{SMC})$

where $k_3 = \operatorname{diag}\{k_{31}, k_{32}, k_{33}\}, k_{31} > 0, k_{32} > 0, k_{33} > 0$, $k_4 = \operatorname{diag}\{k_{41}, k_{42}, k_{43}\}, k_{41} > 0, k_{42} > 0, k_{43} > 0$, $\alpha_2 > 1$,

$$\lvert S_{SMC}\rvert^{\alpha_2} \operatorname{sign}(S_{SMC}) = \left[\left\lvert S_{SMC(1)}\right\rvert^{\alpha_2} \operatorname{sign}(S_{SMC(1)}), \left\lvert S_{SMC(2)}\right\rvert^{\alpha_2} \operatorname{sign}(S_{SMC(2)}), \left\lvert S_{SMC(3)}\right\rvert^{\alpha_2} \operatorname{sign}(S_{SMC(3)})\right]^T,$$

$$\lvert S_{SMC}\rvert^{\alpha_3} \operatorname{sign}(S_{SMC}) = \left[\left\lvert S_{SMC(1)}\right\rvert^{\alpha_{31}} \operatorname{sign}(S_{SMC(1)}), \left\lvert S_{SMC(2)}\right\rvert^{\alpha_{32}} \operatorname{sign}(S_{SMC(2)}), \left\lvert S_{SMC(3)}\right\rvert^{\alpha_{33}} \operatorname{sign}(S_{SMC(3)})\right]^T,$$

additionally, $\alpha_{3i} = \begin{cases} \max\left\{\alpha_2, \left\lvert S_{SMC(i)}\right\rvert\right\}, & \left\lvert S_{SMC(i)}\right\rvert \geq 1 \\ \min\left\{\alpha, \left\lvert S_{SMC(i)}\right\rvert\right\}, & \left\lvert S_{SMC(i)}\right\rvert < 1 \end{cases}, \quad i = 1, 2, 3$

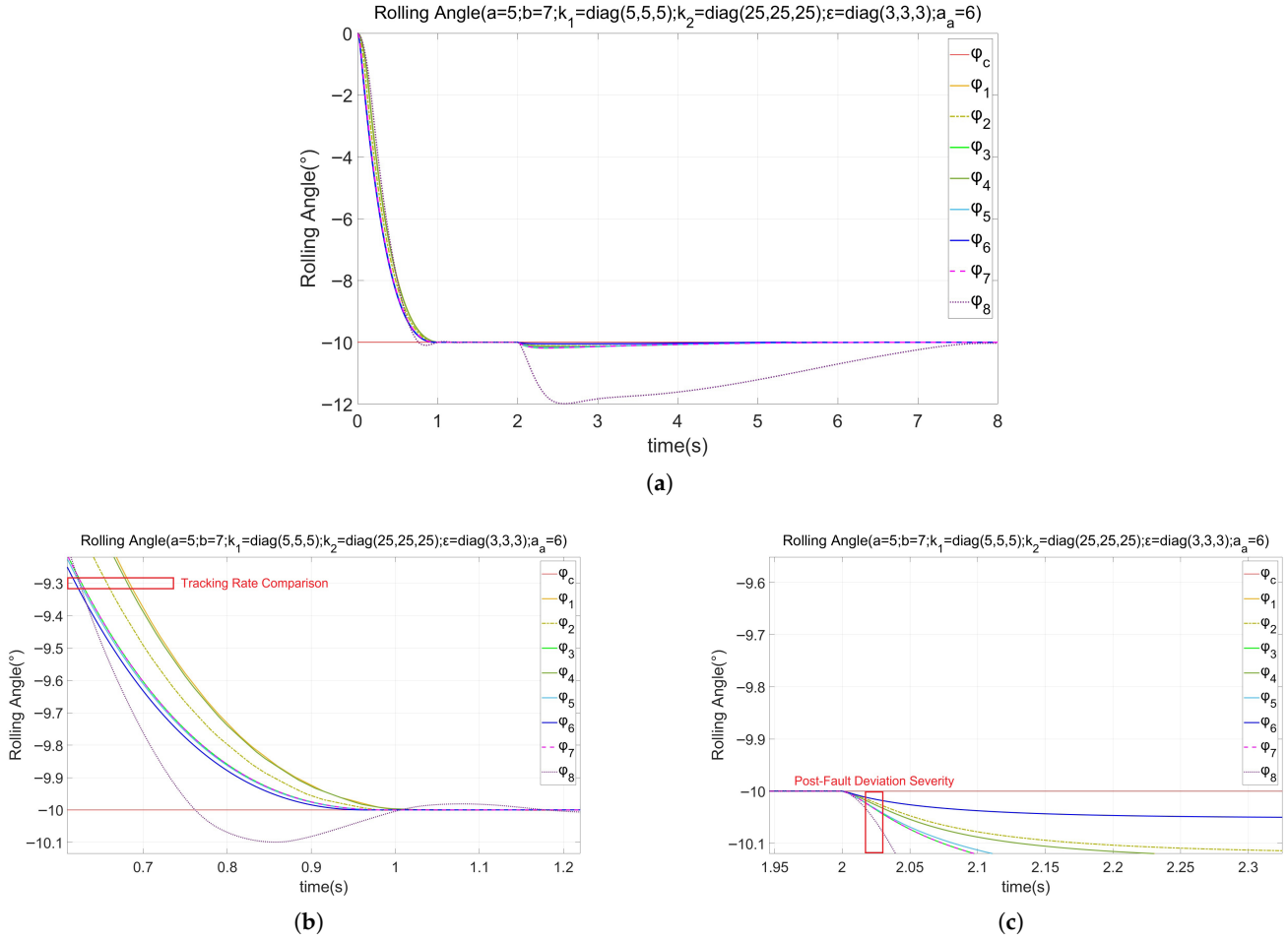


Figure 8. Enlarged partial graph of the launch vehicle rolling angle deviating from the launch vehicle rolling angle tracking-instruction when the parameters of the failure regarding deviation become worse. (**a**) The original simulation graph of the launch vehicle rolling angle. (**b**) The enlarged partial graph of the launch vehicle rolling angle tracking near the launch vehicle rolling angle tracking-instruction before failures occurred. (**c**) The enlarged partial graph of the launch vehicle rolling angle deviating from the launch vehicle rolling angle tracking-instruction after failures occurred.

Let $a = 5$, $b = 7$, $\boldsymbol{k}_1 = \mathrm{diag}\{5,5,5\}$, $\boldsymbol{k}_2 = \mathrm{diag}\{25,25,25\}$, $\boldsymbol{k}_3 = \mathrm{diag}\{25,25,25\}$, $\boldsymbol{k}_4 = \mathrm{diag}\{25,25,25\}$, $\boldsymbol{\varepsilon} = \mathrm{diag}\{3,3,3\}$, $\alpha_2 = 2$. The simulation results are shown in Figure 9.

Figure 9 shows the comparison of the attitude fault-tolerant control performance among the Constant Power Reaching Law (CPRL), the Two Power Reaching Law and The Multi Power Reaching Law. In these figures, φ_6 still represents the rolling angle of the launch vehicle adopted by CPRL, φ_9 and φ_{10} represents the Two Power Reaching Law and The Multi-Power Reaching Law, respectively. It is obviously noted that the fault-tolerant control algorithm with CPRL shows faster convergence velocity and better smoothness, shown in the areas contained by the red boxes in Figure 9b,c.

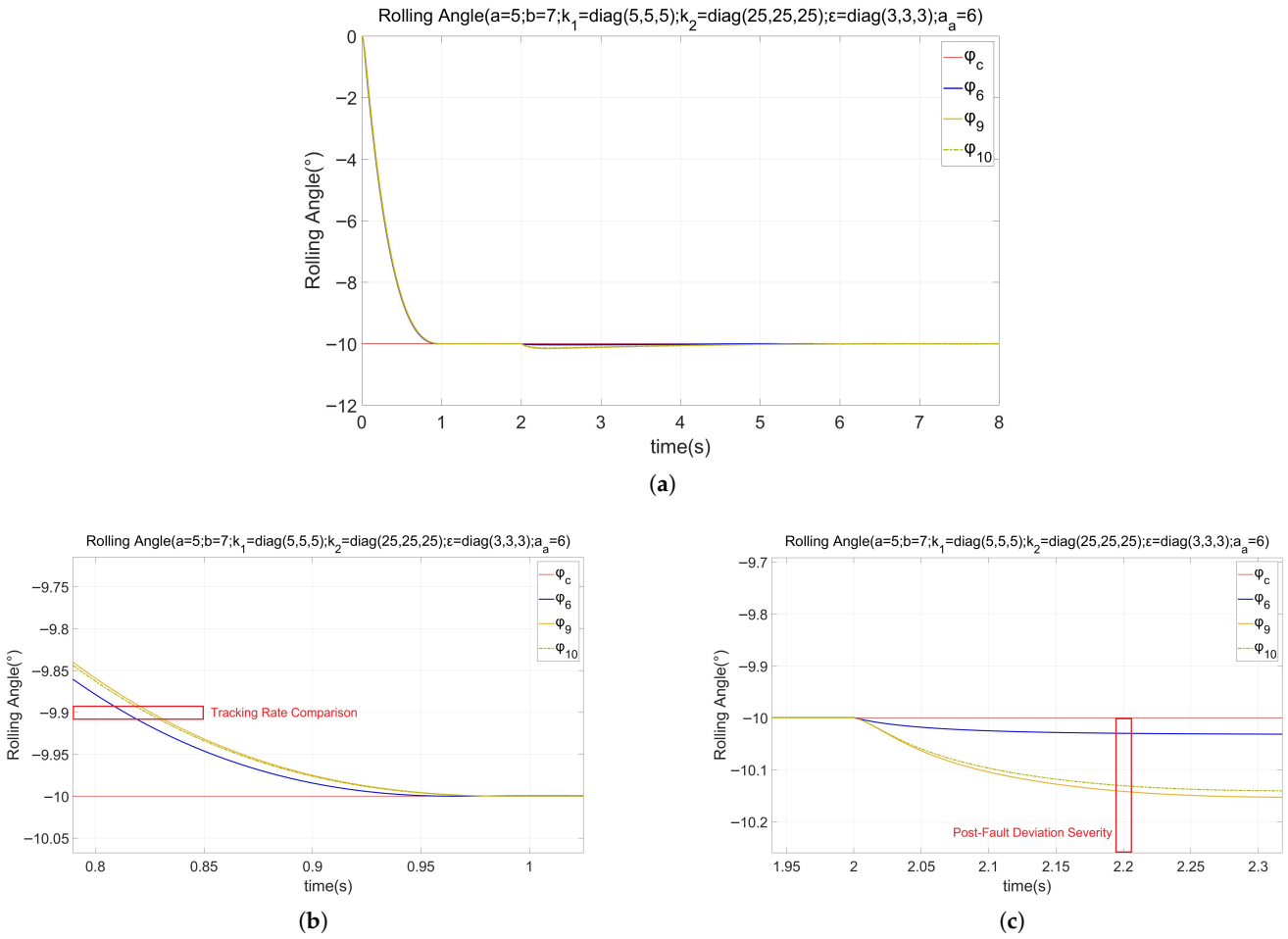


Figure 9. Enlarged partial graph of the launch vehicle rolling angle deviating from the launch vehicle rolling angle tracking-instruction as the controlling performance from the constant Power Reaching Law (CPRL) compares with that from the Two Power Reaching Law and the Multi Power-Reaching Law. (**a**) The original simulation graph of the launch vehicle rolling angle. (**b**) The enlarged partial graph of the launch vehicle rolling angle tracking near the launch vehicle rolling angle tracking-instruction before failures occurred. (**c**) The enlarged partial graph of the launch vehicle rolling angle deviating from the launch vehicle rolling angle tracking-instruction after failures occurred.

4. Conclusions

In the light of the difficulty of harmonizing the response speed and operational stability of the launch vehicle attitude angles in the design of launch vehicle attitude fault-tolerant control when the launch vehicle actuator failures occurred, by means of investigation into the mutual relationship between a series of parameters—including rise time, maximum overshoot, and transition process time—and dynamic system qualities including response speed and operation stability, a CEIF with the structure including the power exponential function was designed, and a novel CPRL was devised.

The experimental results showed that the calculation results of the CEIF designed in this article could conform with the laws achieved by immediately examining the simulation results. With the help of the CPRL, the fault-tolerant controlling performance indicates that the response speed and operational stability of the launch vehicle attitude angles achieves a two-orders-of-magnitude optimization compared with the suboptimal one before the fault occurred. Even if faults occurred, this performance could still be improved by more than one-third.

Author Contributions: Conceptualization, W.F.; methodology, X.T.; software, X.T.; validation, X.T.; formal analysis, X.T.; investigation, X.T.; resources, W.F.; data curation, X.T.; writing—original draft preparation, X.T.; writing—review and editing, W.F.; visualization, X.T.; supervision, J.Y.; project administration, J.Y.; funding acquisition, W.F. All authors have read and agreed to the published version of the manuscript.

Funding: This research received no external funding.

Data Availability Statement: The data supporting this study cannot be publicly shared due to privacy. Further inquiries about the data should be directed to the corresponding author.

Conflicts of Interest: The authors declare no conflicts of interest.

Appendix A

Table A1. Nomenclature.

Symbol	Units	Description
J_{xx}, J_{yy}, J_{zz}	$kg \cdot m^2$	inertia tensor
$\omega_x, \omega_y, \omega_z$	$^\circ/s$	rotating angular rate
φ, ψ, θ	$^\circ$	rolling angle, yawing angle, pitching angle
e_1, e_2, e_3	/	execution efficiency coefficient
ρ_1, ρ_2, ρ_3	/	bias fault coefficient

References

1. Zhang, W. *Dynamics and Control of Launch Vehicles*; China Astronautic Publishing House: Beijing, China, 2015.
2. Guo, J.; Wang, G.; Zhou, J. Attitude Control for Reentry Reusable Launch Vehicle. In Proceedings of the 2016 28th Chinese Control and Decision Conference (CCDC), Yinchuan, China, 28–30 May 2016; pp. 5633–5636.
3. Xiang, Y.; Guo, J.; Tang, S. Fixed-Time Sliding Mode Control for a Reusable Launch Vehicle in Attitude Adjustment Phase Including Actuator Dynamics. In *Proceedings of 3rd 2023 International Conference on Autonomous Unmanned Systems (3rd ICAUS 2023)*; Qu, Y., Gu, M., Niu, Y., Fu, W., Eds.; Lecture Notes in Electrical Engineering; Springer: Singapore, 2024; Volume 1176, pp. 226–236. Available online: https://link.springer.com/book/10.1007/978-981-97-1099-7 (accessed on 3 January 2026).
4. Liu, J.B. Data-Driven Rocket Flight Attitude Control Research. Master's Thesis, Beijing Jiaotong University, Beijing, China, 2020. [CrossRef]
5. Lu, Y. Space launch vehicle's development in China. *Astronaut. Syst. Eng. Technol.* **2017**, *1*, 1–8.
6. Celani, F. Global and robust attitude control of a launch vehicle in exoatmospheric flight. *Aerosp. Sci. Technol.* **2018**, *74*, 22–36. [CrossRef]
7. Song, Z.Y. The Survey of Launch Vehicle Long Distance Fault Diagnosis Technique. *J. Astronaut.* **2016**, *37*, 135–144. [CrossRef]
8. Shen, Y.; Li, L.L.; Wang, Z.H. A review of fault diagnosis and fault-tolerant control techniques for spacecraft. *J. Astronaut.* **2020**, *41*, 647–656. [CrossRef]
9. Xiao, B. Fault Tolerant Attitude Control for Spacecraft with Actuator Failure. Ph.D. Thesis, Harbin Institute of Technology, Harbin, China, 2014. [CrossRef]
10. Asadi, D. Actuator Fault Detection, Identification, and Control of a Multirotor Air Vehicle Using Residual Generation and Parameter Estimation Approaches. *Int. J. Aeronaut. Space Sci.* **2024**, *25*, 176–189. [CrossRef]
11. Chen, Z.M.; Wang, Z.Y.; Zhang, J.G. *Sliding Mode Variable Structure Control Theory and Application*; Publishing House of Electronics Industry: Beijing, China, 2012.
12. Li, H.J.; Cai, Y.L. Sliding mode control with double power reaching law. *Control Decis.* **2016**, *31*, 498–502. [CrossRef]
13. Zhang, H.X.; Fan, J.-S.; Meng, F.; Huang, J.-F. A new double power reaching law for sliding mode control. *Control Decis.* **2013**, *28*, 289–293. [CrossRef]
14. Zhou, T. Adaptive sliding control based on a new reaching law. *Control Decis.* **2016**, *31*, 1335–1338. [CrossRef]
15. Tong, K.W.; Zhang, X.; Zhang, Y.; Xie, Z.; Cao, R.-X. Sliding Mode Variable Structure Control of Permanent Magnet Synchronous Machine Based on a Novel Reaching Law. *Proc. CSEE* **2008**, *28*, 102–106. [CrossRef]
16. Ge, C.; Li, W.; Huang, Z.; He, J.; Ma, C. Path tracking lateral control strategy based on fuzzy terminal sliding mode controller. *J. Dalian Univ. Technol.* **2024**, *64*, 376–383. [CrossRef]
17. Mei, H.; Wang, Y. Fast Convergent Sliding Mode Variable Structure Control of Robot. *Inf. Control* **2009**, *38*, 552–557. [CrossRef]
18. Zhang, Y.; Ma, G.-F.; Guo, Y.-N.; Zeng, T.-Y. A Multi Power Reaching Law of Sliding Mode Control Design and Analysis. *Acta Autom. Sin.* **2016**, *42*, 466–472. [CrossRef]
19. Mei, X.R. *Automatic Control Principle*, 3rd ed.; Science Press: Beijing, China, 2013.

20. Liang, X.-H.; Hu, C.-H.; Zhou, Z.-J.; Wang, Q. ADP-based intelligent attitude fault-tolerant control for launch vehicles. *Acta Aeronaut. Astronaut. Sin.* **2021**, *42*, 524915. [CrossRef]
21. Zhao, D.-J.; Wang, Y.-J.; Liu, L.; Wang, Z.-S. Robust fault-tolerant control of launch vehicle via GPI observer and integral sliding mode control. *Asian J. Control* **2013**, *15*, 614–623. [CrossRef]
22. Li, Z.-Q.; Tang, B.-W.; Yang, H.; Huang, L.-J. Distributed Global Fast Terminal Sliding Mode Control Strategy for High-speed Train. *J. China Railw. Soc.* **2023**, *45*, 41–50. [CrossRef]

Disclaimer/Publisher's Note: The statements, opinions and data contained in all publications are solely those of the individual author(s) and contributor(s) and not of MDPI and/or the editor(s). MDPI and/or the editor(s) disclaim responsibility for any injury to people or property resulting from any ideas, methods, instructions or products referred to in the content.